Check for updates

Organic–inorganic hexahalometalate-crystal semiconductor K_2(Sn, Se, Te)Br_6 hybrid double perovskites for solar energy applications

K. Bouferrache,[ab] M. A. Ghebouli,[ac] B. Ghebouli,[d] M. Fatmi [ID] *[a] and Sameh I. Ahmed*[e]

Hybrid organic, halide, and divalent metal double perovskites K_2(Sn, Se, Te)Br_6 with cubic structures were computationally evaluated using the generalized-gradient approximation (GGA) and modified Becke–Johnson (mBJ-GGA) functionals. The Goldschmidt tolerance factor, octahedral factor, Helmholtz free energy, and formation energy illustrated the structural, chemical, and thermodynamic stabilities of the studied compounds. The equilibrium lattice constants for K_2SeBr_6 and K_2SnBr_6 deviated from the experimental values by 4.3% and 3.1%, respectively. The elastic constants of K_2(Sn, Se, Te)Br_6 were significantly smaller due to their larger reticular distances, lower Coulomb forces, and reduced hardness. The high dynamic lattice anharmonicity of K_2(Sn, Se, Te)Br_6 reduced their electronic conductivity, providing a practical advantage in the presence of a thermoelectric field. K_2(Se, Te)Br_6 were predicted to have indirect bandgaps of X–L nature, while K_2SnBr_6 exhibited a direct Γ–Γ bandgap. The power conversion efficiency (PCE) for photovoltaic devices with K_2(Sn, Se, Te)Br_6 perovskite compounds as solar absorbers reached 20.51%. Their absorption in the visible region provided an advantage in energy harvesting. The electronic transitions in the studied double perovskites took place between the Br-4p and K-4s orbitals. Thus, these hybrid organic–inorganic halide perovskites proved to be excellent semiconductors for photovoltaic applications and demonstrated optimized photovoltaic efficiency.

1. Introduction

Hybrid double perovskites constitute an important area of research in the photovoltaic field and electroluminescent devices as they have similar characteristics to conventional semiconductors but are cost-effective and offer high energy-conversion efficiencies. These materials are natural multiple quantum wells consisting of alternating organic and inorganic elements. These compounds are a class of semiconductors that combine the advantages of organic (low cost) and inorganic (high performance) semiconductors. The constituents used in these compounds, including K, Sn, Se, Te and Br, and the manufacturing methods are inexpensive.[1] The high absorption coefficient of this type of double perovskites enables them to absorb in the entire visible solar spectrum.[2] These materials show strong photoluminescence (417 Cd m^{-2}) at room

temperature.[3] Hybrid double perovskites K_2(Sn, Se, Te)Br_6 have growing interest in the field of solar cells, and as light-emitting materials, they allow the modulation of emission wavelength throughout the visible range due to the nature of the metal (Sn, Se, Te) and the halogen used (Br). Notably, hybrid double perovskites with bromoplumbate networks emit white light with photoluminescence quantum yields, reaching a value of up to 9%.[4] Some cubic double perovskites with adequate charge transport characteristics have been studied as solar cell absorbers.[5] Hybrid organic–inorganic double perovskites are materials that contain earth-abundant materials with semiconductor properties, such as appropriate bandgap and exceptional light absorption.[6,7] C. Li *et al.* introduced the K_2(Sn, Se, Te)Br_6 double perovskites and estimated their structure geometrically based on the Goldschmidt tolerance factor and octahedral factor.[8] The organic cation structure of hybrid double perovskites affects the diffusion and stability of ions, and their presence between two adjacent unit cells of an inorganic metal halide octahedron. This structure is linked by weak van der Waals interactions.[9] The band structures of double perovskites K_2SeBr_6 and K_2TeBr_6 were calculated by employing spin-polarized HSE06-and PBE-GGA-based density functional theory using the Projector Augmented Wave (PAW) method, as implemented in the Vienna *Ab initio* simulation package (VASP), show indirect bandgaps of 2 eV and 2.42 eV, respectively.[10] The K_2(Sn, Se, Te)Br_6 tetragonal variants have been investigated

[a]Research Unit on Emerging Materials (RUEM), University Ferhat Abbas of Setif 1, Setif, 19000, Algeria. E-mail: fatmimessaoud@yahoo.fr

[b]Department of Physics, Faculty of Sciences, University of M'sila University Pole, Road Bourdj Bou Arreiridj, 28000, M'sila, Algeria

[c]Department of Chemistry, Faculty of Sciences, University of M'sila University Pole, Road Bourdj Bou Arreiridj, 28000, M'sila, Algeria

[d]Laboratory for the Study of Surfaces and Interfaces of Solid Materials (LESIMS), University Ferhat Abbas of Setif 1, Setif, 19000, Algeria

[e]Department of Physics, College of Sciences, Taif University, P. O. Box 11099, Taif 21944, Saudi Arabia. E-mail: sameh2977@gmail.com

computationally within the frameworks of the density functional theory and other functionals, such as HSE06, for potential photovoltaic applications.[11] K_2TeBr_6 double perovskite can take the monoclinic structure, with space group $P2_1{}^n$ ($C_{2h}{}^5$) and lattice parameters $a = 7.521$ Å, $b = 7.574$ Å, $c = 10.730$ Å, and $\beta = 89° 40'$.[12] Moreover, in a systematic investigation of tetragonal and monoclinic $K_2(Sn, Se, Te)Br_6$ based on the density functional theory using the norm-conserving pseudo-potential plane wave method, as implemented in the ABINIT package, the Helmholtz free energies of K_2SnBr_6 indicated a phase transition temperature of 433 K for cubic ($Fm\bar{3}m$) to tetragonal ($P4/mnc$) and 301 K for tetragonal ($P4/mnc$) to monoclinic ($P2_1/n$).[13] Further, the $K_2(Sn, Se, Te)Br_6$ structures have been investigated using other codes, such as CASTEP, ABINIT and VASP, other phases like monoclinic and tetragonal structures and other functionals.[13–18] In this work, we studied hybrid double perovskites with the general chemical formula of $K_2(Sn, Se, Te)Br_6$, where K site cation was organic, Br represented the halide ion and (Sn, Se, Te) were divalent metal cations. We investigated for new double perovskites having adequate optoelectronic characteristics, such as strong absorption in the ultraviolet region and suitable band gap and a power conversion efficiency, which favored the application of these materials in solar cells. Moreover, we identified a suitable analysis technique (Wien2K) and appropriate functionals (mBJ-GGA and HSE06) to evaluate novel double perovskites with suitable structural, optoelectronic and thermoelectric properties for solar cell applications.

2. Methods and computational details

An in-depth study of structural, elastic, electronic and optical calculations requires the use of the WIEN2k code.[19] In this work, phonon dispersion was performed using Phonopy, and the BoltzTrap code was used to study the thermoelectric characteristics. The GGA approach was used to calculate the product of the smallest muffin-tin sphere radius with the largest plane wave vector (K_{max}). The optimization of lattice constants was performed using the generalized gradient approximation (PBE-GGA)[20] of Perdew, Burke, and Ernzerhof. To investigate the electronic, optical, and thermoelectric properties of $K_2(Sn, Se, Te)Br_6$, we employed the Becke–Johnson exchange potential (mBJ).[21] To ensure optimal energy convergence, the GGA approach was applied to calculate the product of the smallest muffin-tin sphere radius (R_{MT}) and the largest plane wave vector (K_{max}), as well as the R_{MT} values of each constituent element (K, Sn, Se, Te, and Br) and the k-points, as detailed in Table 1. For the calculation of optical and thermoelectric properties, a k-mesh of 10 000 points was used, while 5000 points were employed for the elastic constants. The maximum radial expansion was set to $I_{max} = 10$ for self-consistent calculations. The energy cutoff (E_{cut}) between the valence states and the nucleus was set at -8 Ry, and the charge convergence criterion was chosen as 10^{-3} e. In this study, the valence electrons were considered as those that form chemical bonds, while core electrons were those that contribute to the chemical reactivity of the atom. The electronic configurations of the elements involved were as follows: K: [Ar] $4s^1$, Sn: [Kr] $4d^{10} 5s^2 5p^2$, Se: [Ar] $3d^{10} 4s^2 4p^4$, Te: [Kr] $4d^{10} 5s^2 5p^4$, and Br: [Ar] $3d^{10} 4s^2 4p^5$. Notably, the R_{MT} values had a negligible effect on the electronic properties while using the GGA-mBJ exchange potential. The GGA-mBJ method improved the accuracy of key parameters, such as formation energy, transition energy levels, lattice constant, electrostatic potential, valence band maximum, and total energy. The formation energy of a compound corresponds to the energy required to dissociate it into isolated atoms when all chemical bonds are broken.

3. Results and discussion

3.1. Structural stability, elastic constants and mechanical characteristics

The $K_2(Sn, Se, Te)Br_6$ double perovskites form a face-centered cubic structure with space group $Fm\bar{3}m$ (#225). The K, (Sn, Se, Te) and Br atoms are located between the octahedrons 8c (0.25, 0.25, 0.25) at 4a (0, 0, 0) and 24e ($x = 0.2296$, 0, 0). The Goldschmidt tolerance factor and octahedral factor deduced using the formulae $t = \dfrac{(r_K + r_{(Sn,Se,Te)})}{\sqrt{2}(r_{(Sn,Se,Te)} + r_{Br})}$ [22] and $u = \dfrac{r_{(Sn,Se,Te)}}{r_{Br}}$ [23] are around $t \approx 0.9$ and $\mu \approx 0.25 - 0.36$, verifying their structural stability in the cubic phase, where r_K, $r_{(Sn, Se, Te)}$ and r_{Br} are the ionic radii of the K ions, (Sn, Se, Te) and Br sites. Goldschmidt tolerance factor is a significant parameter that determines structural stability in the cubic phase.[24] The values of the Goldschmidt tolerance factor and octahedral factor listed in Table 1 reflect the stability of the hybrid double perovskites under study. A tolerance factor in the range of 0.8 to 1 allows the formation of perovskite structures in the stable cubic phase.[13] Other criteria for other types of double perovskites are summarized elsewhere.[25–27] Their optimization was carried out by plotting energy as a function of volume, as displayed in Fig. 1. Notably, the structural stability of K_2SeBr_6, K_2SnBr_6 and K_2TeBr_6 were observed at energy levels of -38549.32 eV, -46047.29 eV and -40282.73 eV, which corresponded to volumes of 2075 $(a.u)^3$, 2150 $(a.u)^3$ and 2225 $(a.u)^3$, respectively.

Table 1 $R_{MT} \cdot K_{max}$, R_{MT} of the constituents and k-point, Goldschmidt tolerance factor and octahedral factor of $K_2(Sn, Se, Te)Br_6$ calculated using GGA

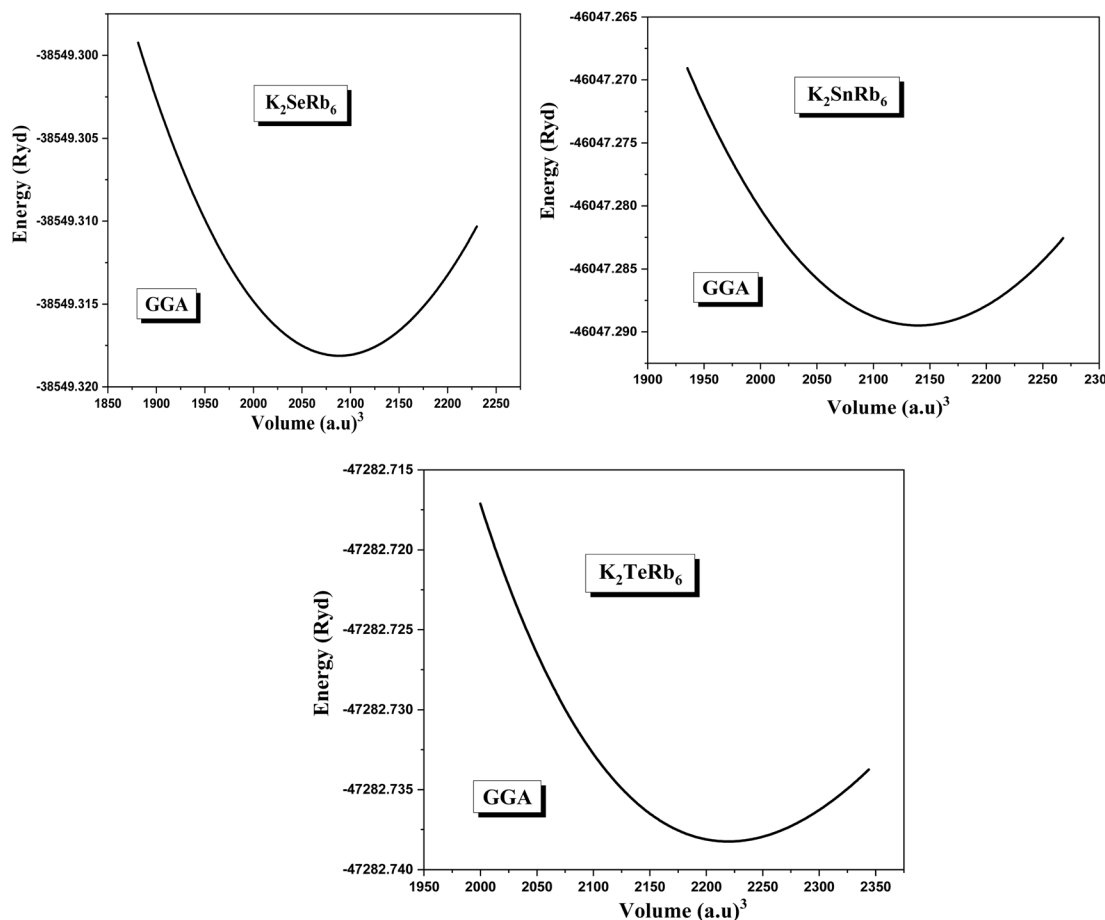|	$R_{MT} \cdot K_{max}$	R_{MT} (K)	R_{MT} (Se, Sn, Te)	R_{MT} (Br)	k-point	t-factor	μ-factor
K_2SeBr_6	9	2.50	2.45	2.45	1000	0.99	0.255
K_2SnBr_6	9	2.50	2.50	2.43	1000	0.925	0.348
K_2TeBr_6	9	2.50	2.50	2.50	1000	0.916	0.362

Fig. 1 Energy *vs.* volume curves for optimizing $K_2(Sn, Se, Te)Br_6$ using GGA approximation.
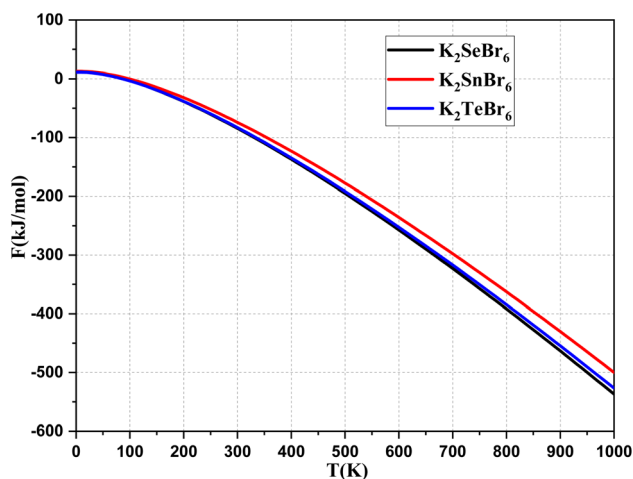

Fig. 2 Helmholtz free energy *vs.* temperature curves of $K_2(Sn, Se, Te)Br_6$ computed by Phonopy using harmonic approximation.

Thus, structural stability is more pronounced for K_2SeBr_6. The convergence test was performed by gradually increasing the density of *k*-points and calculating the total energy of the system for each value. The optimal *k*-point values were selected when the total energy stabilized without a significant change. Fig. 2

shows the Helmholtz free energy of $K_2(Sn, Se, Te)Br_6$ with varying temperatures, as computed by Phonopy in the harmonic approximation. These hybrid perovskites are thermodynamically stable beyond 100 K, with K_2SnBr_6 displaying the best stability. The phonon dispersion curves and their projected density of states were computed, as shown in Fig. 3. The negative frequency phonon modes indicate that these hybrid double perovskites are dynamically unstable. Dynamic instability corresponds to long wavelengths of the phonon spectrum (low pulsations) and frequencies in the first Brillouin zone. The acoustic phonon modes originate mainly from the Br valence electrons, with a less significant contribution from the K and (Sn, Se and Te) valence electrons. The acoustic mode of $K_2(Sn, Se, Te)Br_6$ is governed by the vibrations of the Br and (Sn, Se, Te) atoms in the same direction. The dynamic instability of these double perovskites in the cubic phase means that they are more dynamically stable in another phase.

Phonon modes with negative frequencies in the cubic phase indicate dynamical instability, suggesting a phase transition at low temperatures. We focused on the cubic phase and did not examine other phases, such as tetragonal or monoclinic. However, the study of these phases is crucial for a thorough understanding of crystal stability. This instability results from a non-conservative force due to the vibrations of the acoustic
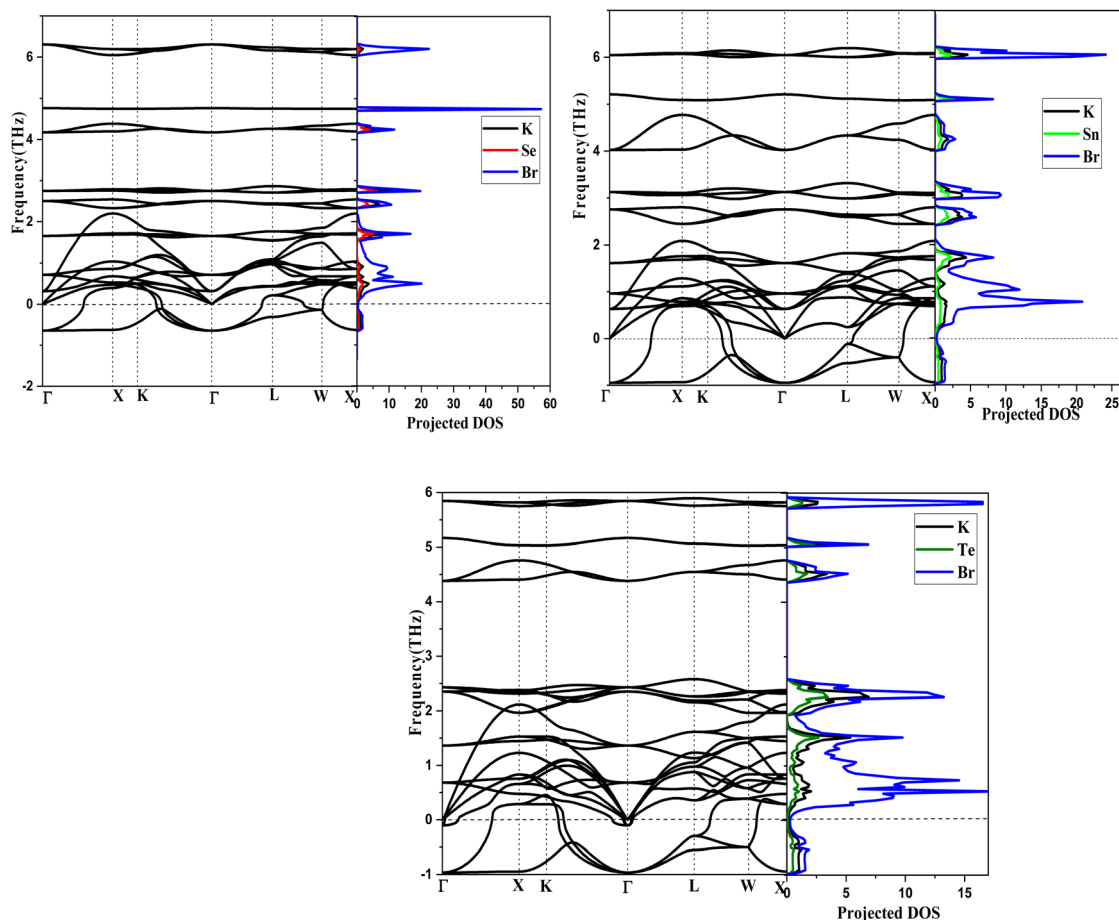
Fig. 3 Phonon dispersion curves and projected density of states of $K_2(Sn, Se, Te)Br_6$.

phonons. The symmetry points of phononic bands differ from one code to another. The transition point L does not affect dynamic instability.[13] The high anharmonic lattice dynamics of $K_2(Sn, Se, Te)Br_6$ reduce electronic conductivity, giving them an advantage for use in the thermoelectric field. Table 2 summarizes the lattice constant, bulk modulus and its derivative with respect to pressure, as well as the minimum and formation energies. The negative formation energies of $K_2(Sn, Se, Te)Br_6$ were used in the following expression to calculate their chemical stabilities:

$$E_{form}^{K_2(Sn,Se,Te)Br_6} = E_{tot}^{K_2(Sn,Set,Te)Br_6} - \frac{E_{tot}^{K}}{2} - E_{tot}^{(Sn,Se,Te)} - \frac{E_{tot}^{Br}}{6} \quad (1)$$

Six decimal digits have been retained in the Rydberg energy values shown in Table 2 for better precision, which is essential because small variations in total energy have a significant impact on the structural stability, phase transitions and formation energy. Our calculated equilibrium lattice constant values for K_2SeBr_6 and K_2SnBr_6 show deviations of 4.3% and 3.1%, respectively, from the experimental values.[28–30] However, the lattice constant value of $K_2(Sn, Se)Br_6$ agreed well with the theoretical values.[17,31] Elastic stiffness constants of materials are the most representative data of the overall elastic and mechanical aspects of related materials. These compounds show weaker elastic constants, which explains their lower hardness. The mechanical analysis and properties of the cubic

Table 2 Lattice constant (a_0), bulk modulus (B), pressure derivative of the bulk modulus B', minimum energy E_0 and formation energy (E_{from}) of $K_2(Sn, Se, Te)Br_6$

	a_0 (Å)	B (GPa)	B'	E_0 (Ry)	$E_{formation}$ (eV)
K_2SeBr_6	10.7369 Exp. 10.363 (ref. 28) 10.2653 (ref. 17)	25.0116 15.35 (ref. 17)	1.5003	−38549.318115	−2.39
K_2SnBr_6	10.8243 Exp. 10.48 (ref. 29 and 30) 10.51 (ref. 31)	27.941	1.9961	−46047.289488	−2.66
K_2TeBr_6	10.9574	21.9369	6.564	−47282.738261	−2.42

Table 3 Elastic constants, shear moduli, bulk moduli, anisotropy factors, Young's moduli, Poisson's ratios and B_H/G_H ratios of K_2(Sn, Se, Te)Br_6

	K_2SeBr_6	K_2SnBr_6	K_2TeBr_6
C_{11} (GPa)	64.04	73.94	73.41
C_{12} (GPa)	5.17	5.58	10.42
C_{44} (GPa)	9.66	10.94	9.06
G_v (GPa)	17.56	20.23	18.03
G_R (GPa)	13.21	15.02	12.67
G_H (GPa)	15.39	17.63	15.35
B (GPa)	24.80	28.37	31.42
A	0.32	0.32	0.28
E_V (GPa)	42.63	49.04	45.42
E_R (GPa)	33.65	38.31	33.52
E_H (GPa)	38.25	43.81	39.61
ϑ_V	0.21	0.21	0.25
ϑ_R	0.27	0.27	0.32
ϑ_H	0.24	0.24	0.28
B_H/G_H	1.61	1.61	2.04

double perovskites were determined using the elastic moduli C_{11}, C_{12}, C_{44} and B based on the finite strain theory, as reported in Table 3, which verifies the criteria for their mechanical stability.

$$0\langle C_{11}, 0\langle C_{44}, 0\langle C_{11} - C_{12}, 0\langle C_{11} + 2C_{12}, C_{12}\langle B\langle C_{11} \qquad (2)$$

Table 3 summarizes the bulk and shear moduli, universal anisotropy factors, Young's moduli, Poisson ratios and Pugh

coefficients of the isotropic polycrystalline materials using the Voigt–Reuss–Hill approximation. The lower elastic constants of K_2(Se, Sn, Te)Br_6 reflect their large inter-reticular distances and weaker bonding forces. The low values of bulk modulus and shear and Young's moduli of these double perovskites confirm their lower hardness and rigidity. Poisson ratio values located between 0.21 and 0.32 are associated with the interatomic forces of central types and covalent bonding character. Bonds nature is described by the factor ν, either ionic-covalent (0.21–0.32) in K_2(Sn, Te, Se)Br_6. The Pugh criterion B_H/G_H and universal anisotropy factors indicate that K_2(Sn, Se)Br_6 are ductile and anisotropic, while K_2TeBr_6 is brittle and anisotropic. Fig. 4 displays the effect of orientation on Young's modulus and Poisson's ratio of K_2(Sn, Te, Se)Br_6 visualized using the ELAT software, which revealed an anisotropic nature. These two parameters of the double perovskites under study appear to be anisotropic in all three directions. The universal anisotropy factors (A) of K_2(Sn, Se, Te)Br_6 confirm their anisotropy.

3.2. Electronic characteristics

The bandgap of a material is a decisive parameter in energy-harvesting applications. Fig. 5 presents the energy band structures and the partial and total densities of states for K_2(Sn, Se, Te)Br_6. The total density of states (TDOS) shows the semiconducting profile along with the bandgap value and zero TDOS at the Fermi level. An indirect X–L bandgap is seen in K_2(Se, Te)Br_6, while that of K_2SnBr_6 is direct Γ–Γ. The partial density of
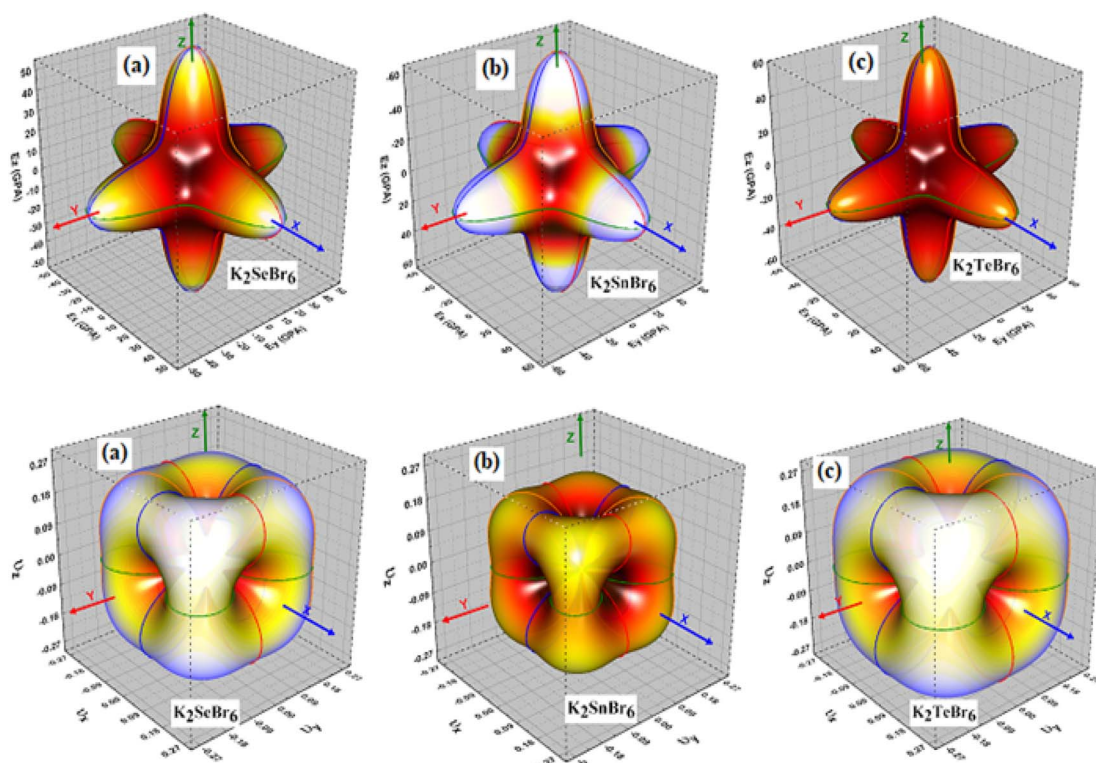

Fig. 4 3D surface maps of Young's modulus (top row) and Poisson's ratio (bottom row) of (a) K_2SeBr_6, (b) K_2SnBr_6 and (c) K_2TeBr_6.
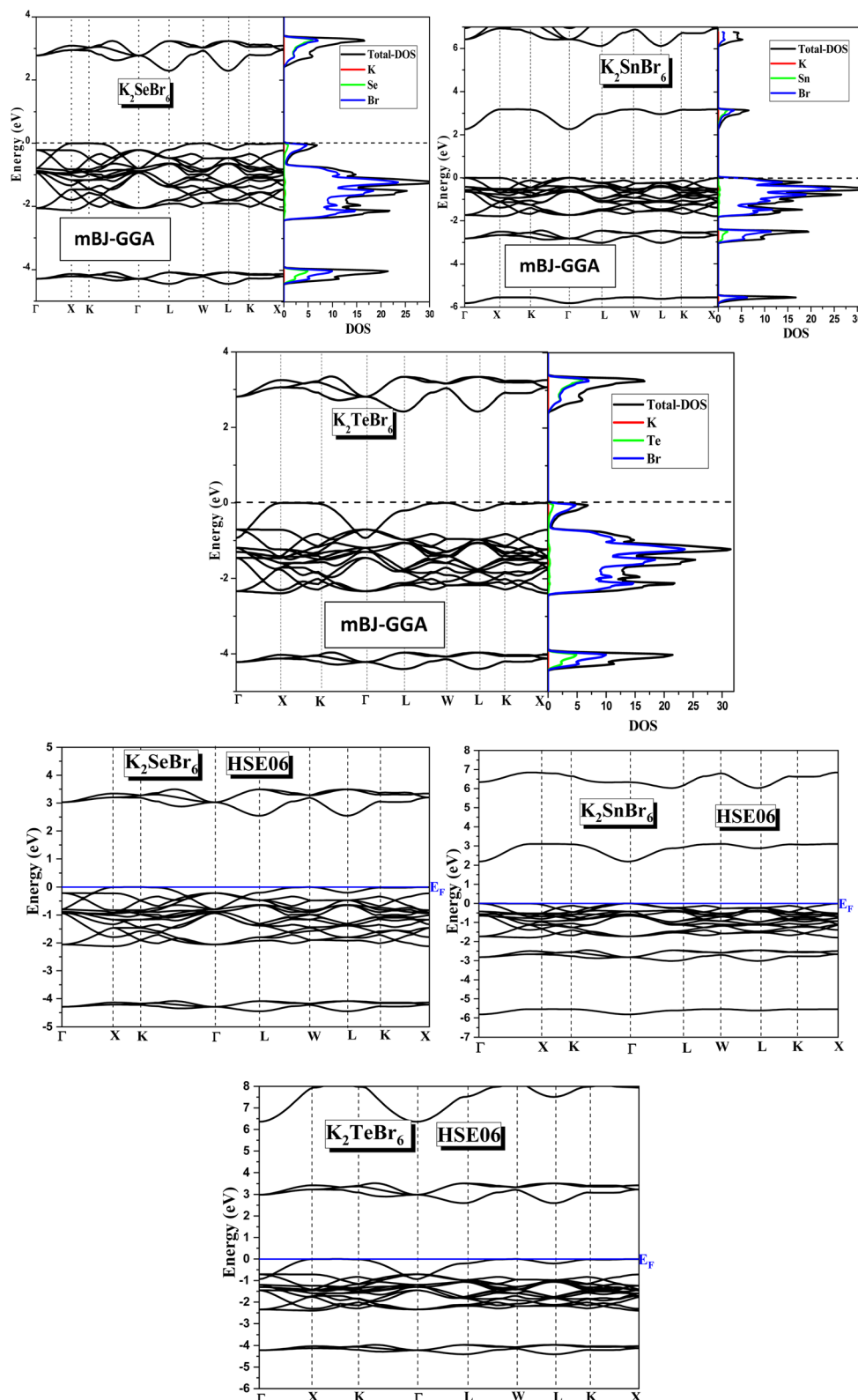
Fig. 5 Electronic band structures and density of states of K_2SeBr_6, K_2SnBr_6 and K_2TeBr_6 calculated using mBJ-GGA and HSE06.

states identifies the different energy bands. The density of states analysis reveals that 4p of Br majorly contributes to the higher valence band, while (5p of Sn, 4p of Se and 5p of Te) and 4p of Br are present in the lower conduction band. All these states define the semiconductive nature of these systems.[27] The bandgap behavior mainly originates from a collective effect of the Br-4p and (5p of Sn, 4p of Se and 5p of Te) states.[24] The contribution to the upper valence band is mainly from the Br-4p

Table 4 Bandgaps (eV) of $K_2(Sn, Se, Te)Br_6$ calculated using GGA and mBJ-GGA

	GGA	mBJ-GGA
K_2SeBr_6	1.676	2.291
K_2SnBr_6	1.135	1.81
		1.81 (HSE06)[31]
K_2TeBr_6	1.954	2.422
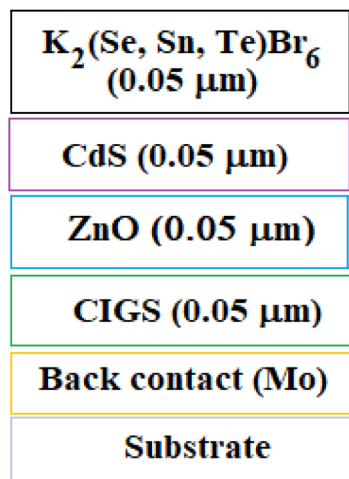
Fig. 6 Solar cell structure.

electrons in all the double perovskites under study. The bottom conduction bands are dominated by the Te-5p, Sn-5p and Se-4p orbitals. The forbidden band in the visible region (1.6 eV to 3.1 eV) of $K_2(Sn, Se, Te)Br_6$ is advantageous for the energy-harvesting property. The first conduction band is empty, and therefore, the electronic transition will take place between the Br-4p orbitals and K-4s in all double perovskites studied. In the $K_2(Sn, Se, Te)Br_6$ crystal structures, the Br–K bond is ionic, while the Br-(Se, Sn, Te) bonds have a covalent tendency. The $K_2(Sn, Se, Te)Br_6$ double perovskites exhibit high dielectric constants and absorption coefficients in the visible and especially,

ultraviolet regions. The underestimation of the bandgap by the GGA functional is due to the binding energy of the Sn-5p, Se-4p and Te-5p levels, hence the use of the mBJ-GGA functional gives better precision. Cubic $K_2(Sn, Se, Te)Br_6$ are suitable for application as light absorbers in solar cell devices due to their appropriate bandgaps of 2.291, 1.81, and 2.422 eV, respectively. The mBJ-GGA-computed bandgap of K_2SnBr_6 is identical to that calculated using the HSE06 functional (1.81 eV).[31] Therefore, HSE06 and mBJ-GGA are the most reliable functionals for band structure calculations. The values of their band gap favor them for use in higher efficiency solar cells. The symmetry points of the electronic bands differ from one code to another. The transition point L does not affect the bandgap.[13]

The accuracy of the bandgap value was confirmed by the Heyd–Scuseria–Ernzerhof hybrid exchange-correlation functional (HSE06), which is the most accurate method. The improvement offered by HSE06 is due to the fact that this short-range functional is partially replaced by the Hartree–Fock exchange. The bandgaps calculated using the GGA, mBJ-GGA and HSE06 functionals are presented in Table 4. The mBJ-GGA functional provides an efficient alternative as it balances accuracy and computational efficiency.

Fig. 6 shows the structure of the solar cell used for simulation; CIGS is the p-type absorber layer, and ZnO and CdS are the n-type buffer layers considered as windows. The highly conductive n-type $K_2(Sn, Se, Te)Br_6$ placed on top is considered the absorber layer. A thin film of Mo is considered the back contact between the substrate and CIGS layer in the simulation. The optimal thickness of the CIGS layer was evaluated to simulate optimal performance. We estimated the thicknesses of the ZnO and CdS windows and the absorber layers in the same manner. The physical parameters of different thin films, including CISSe, ZnO, CdS, and $K_2(Sn, Se, Te)Br_6$, used in the simulation of solar cell structure are reported in Table 5.

We used SCAPS (solar cell capacitance software) as the simulation software. The numerical simulations were done by varying the absorber layer $K_2(Sn, Se, Te)Br_6$. The optimal values of J_{SC} and V_{OC} to obtain improved performance were deduced from the $J–V$ characteristics. The efficiency, fill factor, short current and open-circuit voltage of the different solar cells are

Table 5 Physical parameters of different thin films (CISSe, ZnO, CdS, K_2SeBr_6, K_2SnBr_6 and K_2TeBr_6) used for the simulation of the solar cell structure

Material properties	CIGS	ZnO	CdS	K_2SeBr_6	K_2SnBr_6	K_2TeBr_6
Thickness (μm)	1	0.05	0.05	0.05	0.05	0.05
Band gap (eV)	1.1	3.300	2.4	2.291	2.262	2.422
Electron affinity	4.500	4.100	4.2	4.0	4.0	4.0
Dielectric permittivity	13.6	9.000	10	2.643	3.089	2.395
CB density (cm^{-3})	2.200×10^{18}	4.000×10^{18}	2.2×10^{18}	2.200×10^{18}	2.200×10^{18}	2.200×10^{18}
VB density (cm^{-3})	1.800×10^{19}	1.000×10^{19}	1.8×10^{19}	1.800×10^{19}	1.800×10^{19}	1.800×10^{19}
Electron thermal velocity ($cm\ s^{-1}$)	1.000×10^7	1.000×10^8	1×10^7	1.000×10^7	1.000×10^7	1.000×10^7
Electron thermal velocity ($cm\ s^{-1}$)	1.000×10^7	1.000×10^8	1×10^7	1.000×10^7	1.000×10^7	1.000×10^7
Electron mobility ($cm^2\ V^{-1}\ s^{-1}$)	1.000×10^2	1.000×10^2	1×10^2	1.000×10^2	1.000×10^2	1.000×10^2
Hole mobility ($cm^2\ V^{-1}\ s^{-1}$)	2.500×10^1	2.500×10^1	25	2.500×10^1	2.500×10^1	2.500×10^1
Donor density (cm^{-3})	1.000×10^1	1.000×10^{18}	1×10^{18}	1.000×10^1	1.000×10^1	1.000×10^1
Acceptor density (cm^{-3})	2.000×10^{16}	1.000×10^5	0	2.000×10^{16}	2.000×10^{16}	2.000×10^{16}
Absorption coefficient (cm^{-1})	Scaps value	Scaps value	Scaps value	Scaps value	Scaps value	Scaps value

Table 6 Efficiency, fill factor, short current and open circuit voltage of the simulated solar cells

Thin film solar cell	Efficiency (%)	Fill factor (%)	J_{sc} (mA cm^{-1})	V_{oc} (V)
Sub/Mo/CIGS/ZnO/CdS/K$_2$SeBr$_6$	19.23	60.56	50.61	0.688
Sub/Mo/CIGS/ZnO/CdS/K$_2$SnBr$_6$	18.15	62.59	48.44	0.675
Sub/Mo/CIGS/ZnO/CdS/K$_2$SeBr$_6$	20.51	60.54	52.33	0.695

reported in Table 6. The best power conversion efficiency (PCEs) achieved using K$_2$(Sn, Se, Te)Br$_6$ perovskite compounds as solar absorbers in photovoltaic devices is 20.51%. The solar cell with the K$_2$SeBr$_6$ absorber layer presents the best performance.

3.3. Optical properties

The optical characterization of materials provides valuable insights into their potential application in optoelectronic devices. The real part of the dielectric constant reflects polarization and light dispersion, whereas its imaginary component represents absorption when the incident photon energy exceeds a certain threshold. Fig. 7 illustrates the variations of the real and imaginary parts of the dielectric function, refractive index, extinction coefficient, energy loss, absorption, optical conductivity, and reflectivity as a function of photon energy. For K$_2$SnBr$_6$, K$_2$TeBr$_6$, and K$_2$SeBr$_6$, the static dielectric constant values are 3.1, 2.37, and 2.62, respectively, and reach the maximum values of 5.25 at 3 eV, 3.25 at 3.25 eV, and 4 at 2.8 eV. The relatively low static dielectric constants of K$_2$(Sn, Se, Te)Br$_6$ can be attributed to the contribution of valence electrons (Br, Sn, Se, and Te) to lattice dynamics at energies lower than the bandgap. Additionally, in the ultraviolet region, the real part of the dielectric constant of these double perovskites drops to approximately 0.25. The imaginary part of the dielectric function starts at energies corresponding to the indirect X–L transition for K$_2$(Se, Te)Br$_6$ and the direct Γ–Γ transition for K$_2$SnBr$_6$. The refractive index of a material is directly related to the speed of light propagation and optical transitions. The static refractive index values of K$_2$SnBr$_6$, K$_2$SeBr$_6$, and K$_2$TeBr$_6$ are 1.75, 1.62, and 1.55, respectively. These values reach the maximum values of 2.36, 2.0, and 1.85 before decreasing linearly. Notably, the static refractive index and the dielectric constant strongly correlate with the bandgap. The extinction coefficient, which quantifies the fraction of light lost due to scattering and absorption, follows a trend similar to the imaginary part of the dielectric constant. The absorption coefficient depends on the incident photon energy and becomes significant when this energy equals or exceeds the bandgap. The absorption thresholds closely match the calculated bandgaps and correspond with the interband electronic transitions. While absorption in the visible range is relatively weak, these materials exhibit strong absorption in the ultraviolet region, which makes them promising candidates for solar cell applications. The real part of the optical conductivity begins at energies corresponding to the bandgap for all studied double perovskites. The observed peaks are mainly attributed to interband transitions between the occupied and unoccupied states. The real optical conductivity follows a similar trend to the imaginary

part of the dielectric function, increasing with photon energy. Conversely, the imaginary part of the optical conductivity is negative, indicating possible interband transitions and transport relaxation time effects. Energy loss arises from the conversion of energy from one form to another. In K$_2$(Sn, Se, Te)Br$_6$, energy loss occurs between 0.9 and 1.2 in the ultraviolet region. The optical performance of these compounds is characterized by parameters, such as dielectric function, optical conductivity, refractive index, reflectivity, absorption, and extinction coefficient.[32] The calculated optical conductivity values of K$_2$SeBr$_6$, K$_2$SnBr$_6$, and K$_2$TeBr$_6$ in the visible range are 850 (Ω cm)$^{-1}$, 1000 (Ω cm)$^{-1}$, and 250 (Ω cm)$^{-1}$, respectively, while Co$_x$Sr$_{1-x}$TiO$_3$ exhibits a conductivity of 10^3 (Ω cm)$^{-1}$.[33] The optical properties of these double perovskites suggest their potential for optoelectronic applications.[34] Furthermore, based on their absorption coefficients, energy loss, and conductivity results, K$_2$(Sn, Se, Te)Br$_6$ can be classified as semiconductors.[35]

3.4. Thermoelectric properties

Fig. 8 illustrates the temperature dependence of the Seebeck coefficient, electrical and electronic conductivity (with a relaxation time of $\tau = 0.8 \times 10^{-8}$ s), figure of merit (ZT), and power factor of K$_2$(Sn, Se, Te)Br$_6$, as calculated using the BoltzTraP code.[36] The Seebeck coefficient shows positive values at all temperatures, indicating that the charge carriers are predominantly holes, confirming the p-type semiconducting nature of these double perovskites. For all studied compounds, the Seebeck coefficient decreases with increasing temperature and follows the trend K$_2$TeBr$_6$ → K$_2$SnBr$_6$ → K$_2$SeBr$_6$ in the temperature range of 150 K to 500 K. At 300 K, its values are 190 μV K^{-1}, 200 μV K^{-1}, and 210 μV K^{-1} for K$_2$TeBr$_6$, K$_2$SnBr$_6$, and K$_2$SeBr$_6$, respectively.

Electrical conductivity, which quantifies the ability of a material to conduct electric current, is governed by ohmic conduction *via* electron propagation. It is related to carrier concentration through the equation $\sigma = nq\mu$, where n is the carrier concentration, q is the electronic charge, and μ is the mobility. In K$_2$(Sn, Te)Br$_6$, electrical conductivity increases quadratically with temperature, whereas in K$_2$SeBr$_6$, it exhibits a linear increase. Efficient thermoelectric materials typically exhibit lower electronic conductivity due to phonon–phonon scattering, which is observed in these p-type perovskites. The electronic conductivity of K$_2$(Sn, Se, Te)Br$_6$ increases quadratically with temperature. The efficiency of a thermoelectric material in converting heat into electrical energy is evaluated by the figure of merit (ZT). The estimated ZT values at 300 K are 0.81, 0.78, and 0.77 for K$_2$SnBr$_6$, K$_2$SeBr$_6$, and K$_2$TeBr$_6$, respectively. These values suggest that these materials hold promise for thermoelectric applications. The
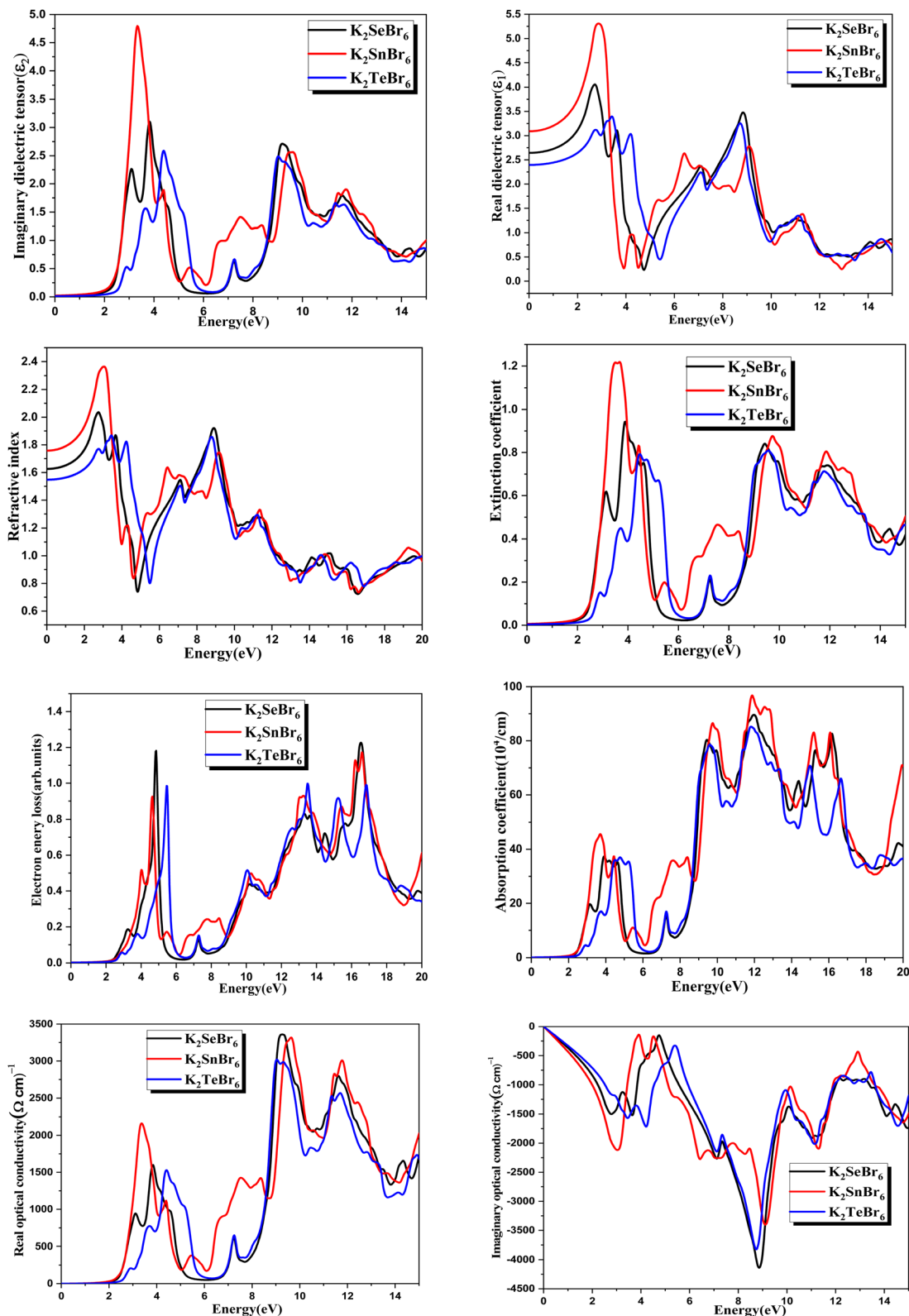
Fig. 7 Real and imaginary parts of the dielectric function, refractive index, extinction coefficient, electron energy loss, absorption coefficient, real and imaginary parts of the optical conductivity of K$_2$(Sn, Se, Te)Br$_6$ as a function of photon energy calculated using mBJ-GGA.

temperature dependence of ZT follows a trend similar to that of the Seebeck coefficient, remaining nearly constant beyond 500 K. However, increasing the temperature leads to a reduction in the

bandgap, which in turn influences ZT and affects thermoelectric performance. The power factor, which describes the real power transmitted along a transmission line relative to the total
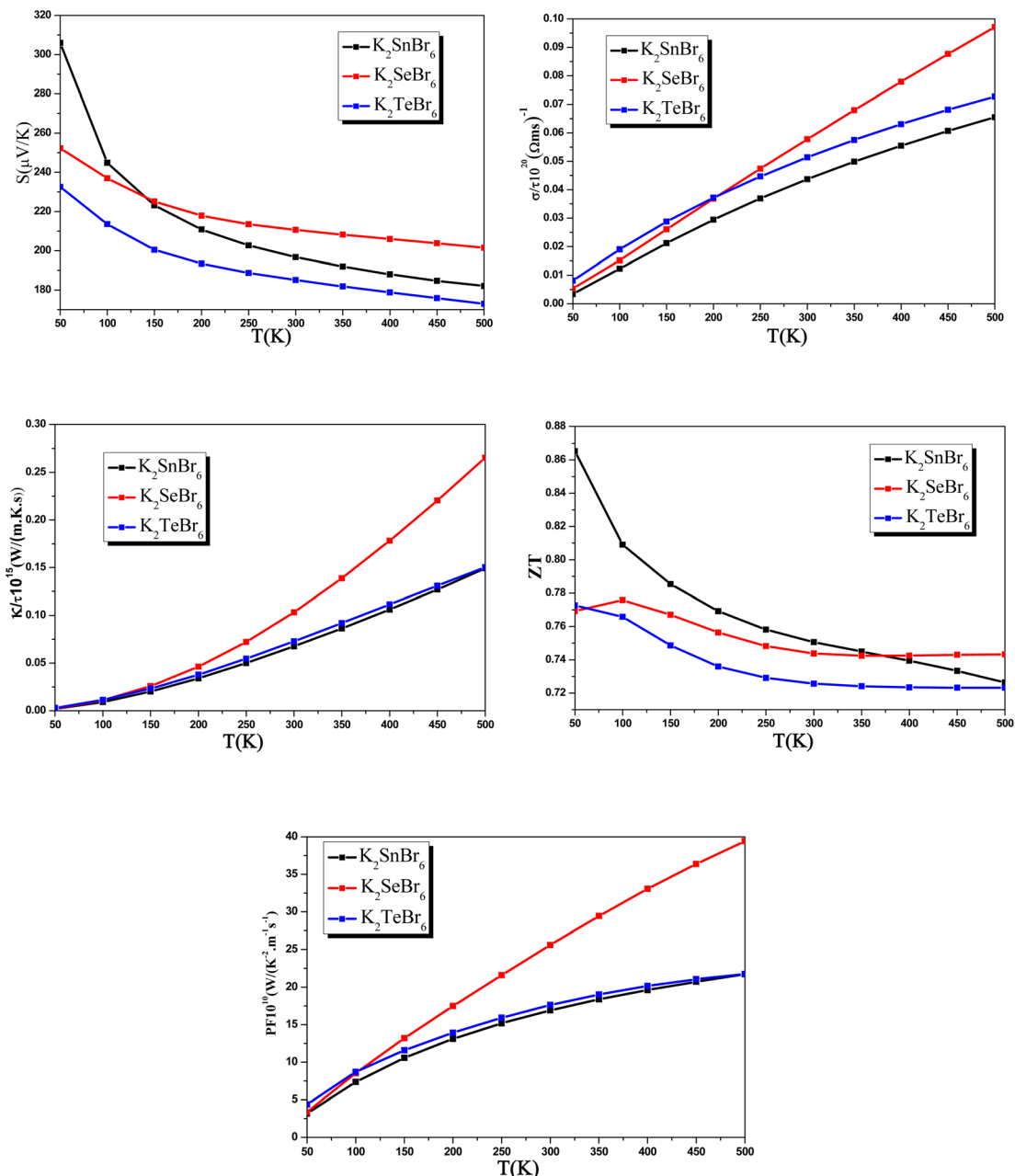
Fig. 8 Temperature dependence of the Seebeck coefficient, electrical conductivity, electronic conductivity, figure of merit ZT and power factor of $K_2(Sn, Se, Te)Br_6$.

apparent power, varies exponentially with temperature for $K_2(Sn, Se, Te)Br_6$. These double perovskites exhibit high absorption coefficients in the visible-ultraviolet spectrum, ranging from 4×10^5 cm^{-1} to 8×10^5 cm^{-1}. Their thermoelectric characteristics reveal remarkable Seebeck coefficients (ranging from 190 to 230 μV K^{-1}) and optical conductivity between 1500 and 2000 Ω^{-1} cm^{-1}, making them highly suitable for application in solar cells and thermoelectric devices. The electrical conductivity, figures of merit, power factors, thermal conductivity, and Seebeck coefficients of these double perovskites calculated using the BoltzTraP code confirm their potential for thermoelectric and optoelectronic applications.[37]

4. Conclusion

The organic–inorganic halide double-perovskite solar cells studied in this work can offer certified power conversion efficiency and are promising candidates for photovoltaic applications. Their acoustic phonon modes originate mainly from the Br valence electrons, with less significant contributions from the K and (Sn, Se and Te) valence electrons. Their positive Seebeck coefficient translate the negative charge carriers, indicating that these double perovskites are p-type semiconductors. Their efficient thermoelectric properties are attributed to lower electronic conductivity, which is linked to phonon–phonon scattering, and the achieved p-type

semiconductors present appropriate figures of merit. The negative imaginary part of the optical conductivity is linked to possible interband transitions and transport relaxation time. Their significant light absorption in the ultraviolet region and adequate bandgaps make these materials ideal for solar cell applications.

Data availability

Data relevant to the results presented in this study are not publicly available at this time but may be obtained from the corresponding author (fatmimessaoud@yahoo.fr) upon reasonable request.

Author contributions

Conceptualization: K. Bouferrache, data curation: M.A. Ghebouli, formal analysis: B. Ghebouli, validation: Sameh I. Ahmed, M. Fatmi.

Conflicts of interest

The authors declared no potential conflicts of interest.

Acknowledgements

References

1 S. Razza, S. Castro-Hermosa, A. Di Carlo and T. M. Brown, *APL Mater.*, 2016, **4**, 091508.

2 W. Yin, T. Shi and Y. Yan, *Adv. Mater.*, 2014, **26**(27), 4653–4658.

3 Y. Kim, H. Cho, J. Hyuck Heo, T.-S. Kim, NoS. Myoung, C.-L. Lee, H. I. Sang and T.-W. Lee, *Adv. Mater.*, 2015, **27**(7), 1248–1254.

4 E. R. Dohner, A. Jaffe, L. R. Bradshaw and H. I. Karunadasa, *J. Am. Chem. Soc.*, 2014, **136**(38), 13154–13157.

5 S. Chadli, A. Bekhti Siad, M. Baira, M. B. Siad, A. Allouche and A. B. Reguig, *Solid State Commun.*, 2022, **342**, 114633.

6 C. C. Stoumpos, C. D. Malliakas and M. G. Kanatzidis, *Inorg. Chem.*, 2013, **52**, 9019–9038.

7 T. M. Brenner, D. A. Egger, L. Kronik, G. Hodes and D. Cahen, *Nat. Rev. Mater.*, 2016, **1**, 15007.

8 C. Li, X. Lu, W. Ding, L. Feng, Y. Gao and Z. Guo, *Acta Crystallogr., Sect. B*, 2008, **64**, 702.

9 C. Li, K. P. Loh and K. Leng, *Matter*, 2022, **5**(12), 4153–4169.

10 H. Kerrai, A. Zaim and M. Kerouad, *Inorg. Chem. Commun.*, 2024, **165**, 112459.

11 Y. Cai, W. Xie, H. Ding, Y. Chen, K. Thirumal, L. H. Wong, N. Mathews, S. G. Mhaisalkar, M. Sherburne and M. Asta, *Chem. Mater.*, 2017, **29**, 77407749.

12 I. D. Brown, *Can. J. Chem.*, 2011, **42**(12), 2758–2767.

13 U. Jong, C. Yu and Y. Kye, *RSC Adv.*, 2020, **10**, 201–209.

14 X. Du, D. He, H. Mei, Y. Liu and N. Cheng, *Mater. Sci. Semicond. Process.*, 2021, **123**, 105579.

15 A. Zikem, H. Baaziz, T. Ghellab, Z. Charifi and F. Soyalp, *Phys. Scr.*, 2024, **99**, 055038.

16 P. D Sreedevi and P. Ravindran, *J. Phys. D:Appl. Phys.*, 2023, **56**(3), 035104.

17 Y. Naceur, H. Bourbaba, M. A. Ghebouli, L. Krache, B. Ghebouli, T. Chihi and M. Fatmi, Sultan Alomairy, *Sci. Rep.*, 2022, **12**, 8345.

18 R. Boudissa, Z. Zerrougui, M. A. Ghebouli, K. Bouferrache, L. Krache, T. Chihi, B. Ghebouli, M. A. Habila, M. Fatmi and M. Sillanpää, *Biophys. Rep.*, 2024, **37**, 101601.

19 K. Bouferrache, M. A. Ghebouli, B. Ghebouli, M. Fatmi, H. Bouandas, T. Chihi, N. H. Alotaibi, S. Mohammad, M. Habila and M. Sillanpää, *J. Mater. Sci. Eng. B*, 2024, **308**, 117550.

20 K. Bouferrache, M. A. Ghebouli, Y. Slimani, B. Ghebouli, M. Fatmi, T. Chihi, A. Djemli, A. Omri, M. D. Albaqami, S. Mohammad, M. Habila and A. Benali, *Solid State Commun.*, 2024, **389**, 115522.

21 A. D. Becke and E. R. Johnson, *A Simple Effective Potential for Exchange* (American Institute of Physics, 2006).

22 M. A. Ghebouli, B. Ghebouli, T. Chihi and M. Fatmi, *Phys. B*, 2021, **610**, 412858.

23 L. Krache, M. A. Ghebouli, B. Ghebouli, S. Alomairy, M. Reffas, M. Fatmi and T. Chihi, *Phys. Status Solidi B*, 2022, **259**(10), 2200042.

24 M. Z. Kazim, M. Ishfaq, S. A. Aldaghfag, M. Zahid and M. Yaseen, *Chem. Phys. Lett.*, 2023, **833**, 140933.

25 M. Ishfaq, S. A. Aldaghfag, M. Zahid, M. Yaseen and N. S. Awwad, *Mater. Chem. Phys.*, 2024, **321**, 129493.

26 M. Ishfaq, M. Yaseen, S. Shukrullah and S. Noreen, *Mater. Chem. Phys.*, 2024, **313**, 128728.

27 M. Z. Kazim, M. Ishfaq, S. A. Aldaghfag, M. Yaseen, M. Khalid and A. Dahshan, *J. Phys. Chem. Solids*, 2024, **185**, 111756.

28 N. Wruk, J. Pelzl, G. A. Saundersn and T. Hailing, *J. Phys. Chem. Solids*, 1985, **46**(11), 1235–1242.

29 H. Boysen and A. W. Hewat, *Acta Crystallogr., Sect. B: Struct. Crystallogr. Cryst. Chem.*, 1978, **34**, 1412–1418.

30 T. Higashi, S. Syoyama and K. Osaki, *Acta Crystallogr., Sect. B: Struct. Crystallogr. Cryst. Chem.*, 1979, **35**, 144–146.

31 U.-G. Jong, C.-J. Yu and Y.-H. Kye, *RSC Adv.*, 2020, **10**, 201–209.

32 M. K. Butt, S. A. Aldaghfag, M. Z. Kazim, M. Yaseen, M. Zahid and M. Ishfaq, *Phys. Status Solidi B*, 2023, **260**(11), 2300206.

33 M. Ishfaq, M. Yaseen, F. F. Al-Harbi and M. K. Butt, *Phys. B*, 2023, **664**, 415025.

34 A. Sohail, S. A. Aldaghfag, M. K. Butt, M. Zahid, M. Yaseen, J. Iqbal, M. Ishfaq and A. Dahshan, *J. Ovonic Res.*, 2021, **17**(5), 461–469.

35 M. Manzoor, M. W. Iqbal, I. Sadique, M. Wabaidur, E. A. Al-Ammar, I. Stoch, R. Sharma and M. Z. Ansari, *Chin. J. Phys*, 2024, **89**, 278–289.

36 G. K. Madsen, D. J. Singh and B. T. P. A. code, *Comput. Phys. Commun.*, 2006, **175**, 67–71.

37 S. A. Aldaghfag, Nasarullah, A. Aziz, M. Ishfaq, M. Yaseen, Hafsa and S. Jamshaid, *Dig. J. Nanomater. Biostructures*, 2024, **9**(1), 295–308.